Gravitational collapse of a massless scalar field

Leonardo Werneck

March, 2020

Contents

List of Figures

1 Introduction

2 Choptuik's original approach – The ADM Equations

In 1993, Matt Choptuik performed numerical simulations of massless scalar fields minimally coupled to gravity and presented evidence for critical phenomena in this system [1]. He considered families of solutions $\mathcal{S}[p]$ with the property that a critical parameter value, p^*, separates solutions containing black holes from those which do not. He also showed that the limit $p \to p^*$ is *universal* (i.e. independent of the type of initial condition), with structure appearing at arbitrarily small time scales. Furthermore, he showed that the masses of the black holes formed in this limit obey the power law $M_{\mathrm{BH}} \propto |p - p^*|^\gamma$, where $\gamma \approx 0.37$ is a universal exponent.

Our goal here is to present a thorough review of the techniques used by Choptuik in his seminal paper, guiding the reader through the steps required to write down a program that is able to reproduce his results. It is important, however, that the reader keep in mind that the techniques used by Choptuik are outdated and specialized to this specific problem, making it harder to generalize the final program to work with different problems. A more extensible and modern approach will be presented in the next section, when we review the problem using the BSSN formalism.

We emphasize that the goal of this section is to discuss the *numerical techniques* needed to solve the problem. This means we will not derive the equations used in detail, but we will present useful references.

2.1 The ADM decomposition of Einstein's field equations

Here we present the equations obtained when decomposing Einstein's equations into its time and spatial componenents, known as the *Arnowitt-Deser-Misner (ADM) decomposition* [2]. Our notation will follow that of Baumgarte and Shapiro [3].

Einstein's field equations are written in the form

$$R_{\mu\nu} - \frac{1}{2} g_{\mu\nu} R = 8\pi T_{\mu\nu} \ , \tag{1}$$

where $g_{\mu\nu}$ is the spacetime metric, $R_{\mu\nu}$ is the Ricci tensor computed from $g_{\mu\nu}$, $R \equiv g^{\mu\nu} R_{\mu\nu}$ is the Ricci scalar, and $T_{\mu\nu}$ is the energy-momentum tensor. Note that we have chosen units such that $G_{\mathrm{N}} = 1 = c$, which are called *geometrized units*.

The decomposition of spacetime into space plus time consists of considering spatial hypersurfaces $\Sigma(t)$ of constant time t which are then evolved in forward in time. The 4-metric $g_{\mu\nu}$ is written as

$$g_{\mu\nu} = \begin{pmatrix} -\alpha^2 + \beta_\ell \beta^\ell & \beta_i \\ \beta_j & \gamma_{ij} \end{pmatrix} , \qquad (2)$$

while the inverse 4-metric is written as

$$g^{\mu\nu} = \begin{pmatrix} -\alpha^{-2} & \alpha^{-2}\beta^i \\ \alpha^{-2}\beta^j & \gamma^{ij} - \alpha^{-2}\beta^i\beta^j \end{pmatrix} , \qquad (3)$$

where α is known as the *lapse function*, β is known as the *shift vector*, and γ_{ij} is the ADM 3-metric, with γ^{ij} its inverse.

The lapse function measures the amount of proper time that elapses while moving from a hypersurface $\Sigma(t)$ to a hypersurface $\Sigma(t + \Delta t)$, with Δt a given time step. The shift vector is responsible for "correcting" the spatial coordinates when moving from $\Sigma(t)$ to $\Sigma(t + \Delta t)$. Given a point point (X, Y, Z) at $\Sigma(t)$, we integrate in time by moving in the normal direction towards the next hypersurface $\Sigma(t + \Delta t)$. However, there is no guarantee that we will arrive at the same spatial point (X, Y, Z). The shift vector then corrects this, by translating the new point to (X, Y, Z). Depending on the choice of folliation, however, this does not happen and therefore $\beta^i = 0$. The spatial 3-metric γ_{ij} lives only at the spatial hypersurfaces and have no time component. See figure 1 for an illustration of the ADM decomposition.
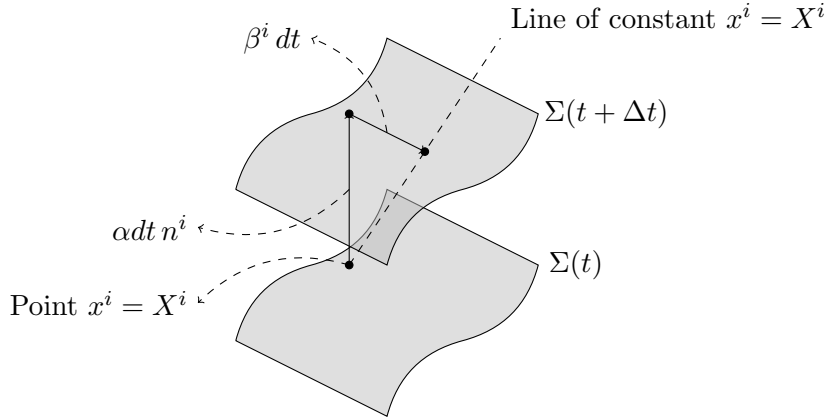
Figure 1: Illustration of the ADM decomposition. In the picture the roles of the lapse function, α, and the shift vector, β^i are depicted, and n^i is the unit vector normal to the hypersurface $\Sigma(t)$. The figure can be misleading, however, because the two surfaces, $\Sigma(t)$ and $\Sigma(t + \Delta t)$, are drawn as exact copies of one another, while in general this is not the case.

The general form of the line element is then (cf. eq. (2.123) in [3])

$$\begin{aligned} ds^2 &= -\alpha^2 dt^2 + \gamma_{ij}\left(dx^i + \beta^i dt\right)\left(dx^j + \beta^j dt\right) \\ &= \left(-\alpha^2 + \beta_\ell \beta^\ell\right) dt^2 + 2\beta_i dt\, dx^i + \gamma_{ij} dx^i dx^j \ . \end{aligned} \qquad (4)$$

With the coordinate choices made above, we have that the *Hamiltonian constraint* (conservation of energy), $\mathcal{H}$, is given by

$$\mathcal{H} \equiv {}^{(3)}R + K^2 - K_{ij}K^{ij} - 16\pi\rho = 0 \ , \tag{5}$$

where ${}^{(3)}R$ is the Ricci scalar computed from γ_{ij}, K_{ij} is the extrinsic curvature of the spatial hypersurface Σ, $K \equiv \gamma^{ij}K_{ij}$ is the trace of the extrinsic curvature, and $\rho \equiv n^\mu n^\nu T_{\mu\nu}$ is the energy density. The *momentum constraints* (conservation of momentum), $\mathcal{M}$, are given by

$$\mathcal{M}_i \equiv D_j K^j{}_i - D_i K - 8\pi S_i = 0 \ , \tag{6}$$

where D_i are covariant derivatives compatible with γ_{ij} and $S_i \equiv -P^\mu{}_i n^\nu T_{\mu\nu}$ are *momentum densities*, with $P^\mu{}_\nu \equiv \delta^\mu{}_\nu + n^\mu n_\nu$ the operator which projects the spacetime components of a tensor onto the spatial hypersurface Σ.

The evolution equations for the extrinsic curvature and the metric are given by

$$\begin{aligned}
\partial_t K_{ij} = {}&\beta^\ell \partial_\ell K_{ij} + K_{i\ell}\partial_j\beta^\ell + K_{j\ell}\partial_i\beta^\ell - D_i D_j\alpha \\
&+ \alpha\left({}^{(3)}R_{ij} + KK_{ij} - 2K_{i\ell}K^\ell{}_j\right) + 4\pi\alpha\left[\gamma_{ij}\left(S - \rho\right) - 2S_{ij}\right] \ .
\end{aligned} \tag{7}$$

and

$$\partial_t\gamma_{ij} = -2\alpha K_{ij} + D_i\beta_j + D_j\beta_i \ , \tag{8}$$

respectively. These 4 equations, (5)-(8), are the *ADM equations*.

Box 1: The ADM equations

Given the 4-metric $g_{\mu\nu}$, the ADM equations are obtained by considering the decomposition

$$g_{\mu\nu} = \begin{pmatrix} -\alpha^2 + \beta_\ell\beta^\ell & \beta_i \\ \beta_j & \gamma_{ij} \end{pmatrix} \ , \quad g^{\mu\nu} = \begin{pmatrix} -\alpha^{-2} & \alpha^{-2}\beta^i \\ \alpha^{-2}\beta^j & \gamma^{ij} - \alpha^{-2}\beta^i\beta^j \end{pmatrix} \ ,$$

where α is the lapse function, β^i the shift vector, and γ_{ij} the physical spatial metric. With the choice of normal vector

$$n_\mu = (-\alpha, 0, 0, 0) \ , \quad n^\mu = \left(\alpha^{-1}, -\alpha^{-1}\beta^i\right) \ ,$$

the ADM equations are written as two conservation equations (constraints) and two

evolution equations. The evolution equations evolve the spatial metric and extrinsic curvature, K_{ij}, and are given by

$$\partial_t \gamma_{ij} = -2\alpha K_{ij} + D_i \beta_j + D_j \beta_i \, ,$$

and

$$\partial_t K_{ij} = \beta^\ell \partial_\ell K_{ij} + K_{i\ell} \partial_j \beta^\ell + K_{j\ell} \partial_i \beta^\ell - D_i D_j \alpha$$
$$+ \alpha \left({}^{(3)}R_{ij} + K K_{ij} - 2 K_{i\ell} K^\ell{}_j \right) + 4\pi\alpha \left[\gamma_{ij} \left(S - \rho \right) - 2 S_{ij} \right] \, .$$

The Hamiltonian constraint (conservation of energy) reads

$$\mathcal{H} \equiv {}^{(3)}R + K^2 - K_{ij} K^{ij} - 16\pi\rho = 0 \, ,$$

while the momentum constraints (conservation of momentum) reads

$$\mathcal{M}_i \equiv D_j K^j{}_i - D_i K - 8\pi S_i = 0 \, , \tag{9}$$

where $\rho \equiv n^\mu n^\nu T_{\mu\nu}$ is the energy density and $S_i \equiv -P^\mu_i n^\nu T_{\mu\nu}$ are *momentum densities*, with $P^\mu_\nu \equiv \delta^\mu_\nu + n^\mu n_\nu$ the operator which projects the spacetime components of a tensor onto the spatial hypersurface.

2.2 The scalar field evolution equations

The gravitational collapse of a massless scalar field is studied by minimally coupling it to gravity, which is described by the action

$$S = \int d^4 x \sqrt{-g} \left[\frac{1}{16\pi} R - \frac{1}{2} g^{\mu\nu} \partial_\mu \phi \partial_\nu \phi \right] \, , \tag{10}$$

where $g^{\mu\nu}$ is the inverse of the physical 4-metric $g_{\mu\nu}$, g is the determinant of $g_{\mu\nu}$, and ϕ is a massless scalar field. The energy-momentum tensor for a massless scalar field is given by

$$T^\phi_{\mu\nu} = -\frac{2}{\sqrt{-g}} \frac{\delta \mathcal{L}_\phi}{\delta g^{\mu\nu}} = \partial_\mu \phi \partial_\nu \phi - \frac{1}{2} g_{\mu\nu} \partial_\alpha \phi \partial^\alpha \phi \, , \tag{11}$$

where $\mathcal{L}_\phi = \frac{\sqrt{-g}}{2} g^{\mu\nu} \partial_\mu \phi \partial_\nu \phi$ is the Lagrangian density of a massless scalar field. We now consider the most general spherically symmetric 4-metric in the polar/radial gauge, whose line element is given by

$$ds^2 = -\alpha^2\left(t, r\right) dt^2 + a^2\left(t, r\right) dr^2 + r^2 d\Omega^2 \ , \tag{12}$$

where we have chosen to write $\gamma_{rr} = a^2$. The coordinate r measures proper surface area, meaning that a sphere of radius R has proper area $4\pi R^2$. The Einstein-Klein-Gordon equation, which is obtained by varying action (10) with respect to ϕ, then reads

$$\partial_t\left(\frac{a}{\alpha}\partial_t\phi\right) = \frac{1}{r^2}\partial_r\left(r^2\frac{\alpha}{a}\partial_r\phi\right) \ . \tag{13}$$

At this point, Choptuik introduces the two auxiliary fields

$$\Phi\left(t, r\right) \equiv \partial_r\phi\left(t, r\right) \ , \ \Pi\left(t, r\right) \equiv \frac{a\left(t, r\right)}{\alpha\left(t, r\right)}\partial_t\phi\left(t, r\right) \ , \tag{14}$$

so that the Einstein-Klein-Gordon equation can be traded by two first-order (in time and space) partial differential equations

$$\partial_t\Phi = \partial_r\left(\frac{\alpha}{a}\Pi\right) \ , \tag{15}$$

$$\partial_t\Pi = \frac{1}{r^2}\partial_r\left(r^2\frac{\alpha}{a}\Phi\right) \ . \tag{16}$$

The energy density, $\rho = n^\mu n^\nu T^\phi_{\mu\nu} = \alpha^2 T^\phi_{tt}$, is given by

$$\rho = \frac{\Phi^2 + \Pi^2}{2a^2} \ . \tag{17}$$

In this coordinate system, $K = K^r{}_r$, and therefore the Hamiltonian constraint is reduced to

$$\mathcal{H} = {}^{(3)}R - 16\pi\rho \ . \tag{18}$$

Our gauge choice implies that the spatial Ricci scalar associated γ_{ij} is given by

$${}^{(3)}R = \frac{4}{ra^2}\left(\frac{\partial_r a}{a} + \frac{a^2 - 1}{2r}\right) \ , \tag{19}$$

which finally imply that the Hamiltonian constraint is given by

$$\mathcal{H} = \frac{4}{ra^2}\left(\frac{\partial_r a}{a} + \frac{a^2 - 1}{2r}\right) - 8\pi\left(\frac{\Phi^2 + \Pi^2}{a^2}\right) \ . \tag{20}$$

Since we know that $\mathcal{H} = 0$ *analytically*, we can write the equation above as a constraint that must be satisfied at each hypersurface, namely

$$\frac{\partial_r a}{a} + \frac{a^2 - 1}{2r} = 2\pi r \left(\Phi^2 + \Pi^2\right) \ . \tag{21}$$

The last equation used by Choptuik follows from the *polar slicing condition* $K^\theta{}_\theta = 0 = K^\varphi{}_\varphi$ for *all* times. This implies that $\partial_t K_{\theta\theta} = 0$, which in turn implies the relation

$$\partial_t K_{\theta\theta} = -D_\theta D_\theta \alpha + \alpha\, {}^{(3)}R_{\theta\theta} + 4\pi\alpha \left[r^2 \left(S - \rho\right) - 2S_{\theta\theta}\right] = 0 \ , \tag{22}$$

leading to the constraint equation[1]

$$\frac{\partial_r \alpha}{\alpha} - \frac{\partial_r a}{a} - \frac{a^2 - 1}{r} = 0 \ . \tag{23}$$

Equations (15), (16), (21), and (23) are equations (3)-(5) in Choptuik's original paper [1].

Box 2: The EKG+ADM equations in the radial/polar gauge

The Einstein-Klein-Gordon equations in the radial/polar gauge,

$$ds^2 = -\alpha^2 \left(t, r\right) dt^2 + a^2 \left(t, r\right) dr^2 + r^2 d\Omega^2 \ ,$$

are given by

$$\partial_t \Phi = \partial_r \left(\frac{\alpha}{a}\Pi\right) \ ,$$
$$\partial_t \Pi = \frac{1}{r^2}\partial_r \left(r^2 \frac{\alpha}{a}\Phi\right) \ .$$

The equations that allow us to evolve the lapse α and the rr-component of the spatial metric, $\gamma_{rr} \equiv a^2$, are the Hamiltonian constraint

$$\frac{\partial_r a}{a} + \frac{a^2 - 1}{2r} = 2\pi r \left(\Phi^2 + \Pi^2\right) \ ,$$

and the polar slicing condition $K^\theta{}_\theta = 0 = K^\varphi{}_\varphi$, which imply that $\partial_t K_{\theta\theta} = 0$ and thus

$$\frac{\partial_r \alpha}{\alpha} - \frac{\partial_r a}{a} - \frac{a^2 - 1}{r} = 0 \ .$$

---

[1]The following identities are useful to obtain this relation:

$$S_{ii} = T^\phi_{ii} \ , \quad S = \frac{\left(3\Pi^2 - \Phi^2\right)}{2a^2} \ , \quad {}^{(3)}R_{\theta\theta} = \frac{r}{a^3}\partial_r a + \frac{a^2 - 1}{a^2} \ , \quad D_\theta D_\theta \alpha = \frac{r}{a^2}\partial_r \alpha \ .$$

2.3 Numerical techniques

To solve the equations inside box 2 above, we will use *centered, second-order accurate finite differences* to approximate the derivatives. For a given function f at the point $(t, r) = (n \cdot \Delta t, j \cdot \Delta r)$, where Δt and Δr are the time and radial step sizes, respectively, we introduce the notation $f(n \cdot \Delta t, j \cdot \Delta r) \equiv f_j^n$. Then, the derivatives of f with respect to t and r are approximated using

$$
\begin{aligned}
(\partial_r f)_j^n &\approx \frac{f_{j+1}^n - f_{j-1}^n}{2\Delta r} + \mathcal{O}\left(\Delta r^2\right) ~, \\
(\partial_t f)_j^n &\approx \frac{f_j^{n+1} - f_j^{n-1}}{2\Delta t} + \mathcal{O}\left(\Delta t^2\right) ~.
\end{aligned}
\tag{24}
$$

Another common technique used is to consider derivatives at the *cell-centered* points $n \pm 1/2$ and $j \pm 1/2$, for example

$$
\begin{aligned}
(\partial_r f)_{j+1/2}^{n+1/2} &\approx \frac{f_{j+1}^{n+1/2} - f_j^{n+1/2}}{\Delta r} + \mathcal{O}\left(\Delta r^2\right) ~, \\
(\partial_r f)_{j-1/2}^{n-1/2} &\approx \frac{f_j^{n-1/2} - f_{j-1}^{n-1/2}}{\Delta r} + \mathcal{O}\left(\Delta r^2\right) ~, \\
(\partial_t f)_{j+1/2}^{n+1/2} &\approx \frac{f_{j+1/2}^{n+1} - f_{j+1/2}^n}{\Delta t} + \mathcal{O}\left(\Delta t^2\right) ~, \\
(\partial_t f)_{j-1/2}^{n-1/2} &\approx \frac{f_{j-1/2}^n - f_{j-1/2}^{n-1}}{\Delta t} + \mathcal{O}\left(\Delta t^2\right) ~.
\end{aligned}
\tag{25}
$$

To second-order accuracy, we also consider the *averaging* operations

$$
\begin{aligned}
f_{j\pm1/2}^n &\approx \frac{1}{2}\left(f_{j\pm1}^n + f_j^n\right) + \mathcal{O}\left(\Delta r^2\right) ~, \\
f_j^{n\pm1/2} &\approx \frac{1}{2}\left(f_j^{n\pm1} + f_j^n\right) + \mathcal{O}\left(\Delta t^2\right) ~.
\end{aligned}
\tag{26}
$$

We now begin the *discretization* of the evolution equations inside box 2. The discretization of the EKG equations using finite differences is given by

$$
\frac{\Phi_j^{n+1} - \Phi_j^{n-1}}{2\Delta t} = \frac{1}{2\Delta r}\left[\frac{\alpha_{j+1}^n}{a_{j+1}^n}\Pi_{j+1}^n - \frac{\alpha_{j-1}^n}{a_{j-1}^n}\Pi_{j-1}^n\right] ~,
\tag{27}
$$

$$
\frac{\Pi_j^{n+1} - \Pi_j^{n-1}}{2\Delta t} = \frac{3}{r_{j+1}^3 - r_{j-1}^3}\left[r_{j+1}^2\frac{\alpha_{j+1}^n}{a_{j+1}^n}\Pi_{j+1}^n - r_{i-1}^2\frac{\alpha_{j-1}^n}{a_{j-1}^n}\Pi_{j-1}^n\right] ~,
\tag{28}
$$

where we have used the identity $r^{-2}\partial_r = 3\partial_{r^3}$ before discretizing the evolution equation for Π,

in which case the step size associated with this derivative is $r_{j+1}^3 - r_{j-1}^3$, where the exponent 3 is understood to mean "r cubed" and not "at $n = 3$".

The discretization of the polar slicing condition is also relatively simple. First, the equation is written as

$$\left[\frac{\partial_r \alpha}{\alpha} - \frac{\partial_r a}{a} - \frac{a^2 - 1}{r} \right]_{j+1/2}^{n+1} = 0 \ . \tag{29}$$

Then, using our finite differences and averaging operators, we obtain

$$\frac{\alpha_{j+1}^{n+1} - \alpha_j^{n+1}}{\Delta r} + \frac{1}{2} \left(\alpha_{j+1}^{n+1} + \alpha_j^{n+1} \right) \left\{ \frac{1 - \left[\frac{1}{2} \left(a_j^{n+1} + a_{j+1}^{n+1} \right) \right]^2}{r_{j+1/2}} - \frac{2 \left(a_{j+1}^{n+1} - a_j^{n+1} \right)}{\Delta r \left(a_{j+1}^{n+1} + a_j^{n+1} \right)} \right\} = 0 \ . \tag{30}$$

To obtain the discretization of the Hamiltonian constraint, we first introduce a new variable

$$A_i^j \equiv \ln a_i^j \ , \tag{31}$$

so that we have

$$\frac{A_{j+1}^{n+1} - A_j^{n+1}}{\Delta r} + \frac{\exp\left(A_{j+1}^{n+1} + A_j^{n+1} \right) - 1}{2 r_{j+1/2}}$$
$$- 2\pi r_{j+1/2} \left\{ \left[\frac{1}{2} \left(\Phi_{j+1}^{n+1} + \Phi_j^{n+1} \right) \right]^2 + \left[\frac{1}{2} \left(\Pi_{j+1}^{n+1} + \Pi_j^{n+1} \right) \right]^2 \right\} = 0 \ . \tag{32}$$

This completes the discretization of the EKG+ADM system we are interested in evolving.

> **Box 3: The discretization of the EKG+ADM system of equations**
>
> The second-order accurate, both in time and space, discretization of the EKG+ADM system of equations, found in box 2, is

$$\frac{\Phi_j^{n+1} - \Phi_j^{n-1}}{2\Delta t} = \frac{1}{2\Delta r}\left[\frac{\alpha_{j+1}^n}{a_{j+1}^n}\Pi_{j+1}^n - \frac{\alpha_{j-1}^n}{a_{j-1}^n}\Pi_{j-1}^n\right] \, ,$$

$$\frac{\Pi_j^{n+1} - \Pi_j^{n-1}}{2\Delta t} = \frac{3}{r_{j+1}^2 - r_{j-1}^3}\left[r_{j+1}^2\frac{\alpha_{j+1}^n}{a_{j+1}^n}\Pi_{j+1}^n - r_{i-1}^2\frac{\alpha_{j-1}^n}{a_{j-1}^n}\Pi_{j-1}^n\right] \, ,$$

$$\frac{A_{j+1}^{n+1} - A_j^{n+1}}{\Delta r} + \frac{\exp\left(A_{j+1}^{n+1} + A_j^{n+1}\right) - 1}{2r_{j+1/2}}$$
$$- 2\pi r_{j+1/2}\left\{\left[\frac{1}{2}\left(\Phi_{j+1}^{n+1} + \Phi_j^{n+1}\right)\right]^2 + \left[\frac{1}{2}\left(\Pi_{j+1}^{n+1} + \Pi_j^{n+1}\right)\right]^2\right\} = 0 \, ,$$

$$\frac{\alpha_{j+1}^{n+1} - \alpha_j^{n+1}}{\Delta r} + \frac{1}{2}\left(\alpha_{j+1}^{n+1} + \alpha_j^{n+1}\right)\left\{\frac{1 - \left[\frac{1}{2}\left(a_j^{n+1} + a_{j+1}^{n+1}\right)\right]^2}{r_{j+1/2}} - \frac{2\left(a_{j+1}^{n+1} - a_j^{n+1}\right)}{\Delta r\left(a_{j+1}^{n+1} + a_j^{n+1}\right)}\right\} = 0 \, .$$

2.3.1 SinhSpherical coordinates

We also set up the program in a way that will allow us to push the outer boundary, located at $r = r_{\max}$, a lot further out, so that we do not need to worry about spurious reflections from it. This is done by the change of variables

$$r = A\frac{\sinh\left(\frac{x}{w}\right)}{\sinh\left(\frac{1}{w}\right)} \, , \tag{33}$$

where A and w are free parameters and $x \in [0, 1]$. This new coordinate system will henceforth be called *SinhSpherical coordinates*. Note that A corresponds to $r_{\max}$, since for $x = 1$ we have $r = A$. The parameters w changes the sampling density near small values of r. Note that while the grid structure in the r-coordinate is *non-uniform*, being more densely sampled around $r = 0$ and less densely sampled around $r = r_{\max}$, it is *uniformly* sampled in the x-coordinate. The grid structure is illustrated in figure 2.
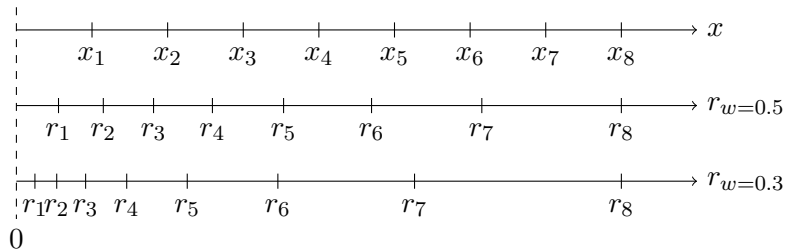

Figure 2: Illustration of the grid structure for SinhSpherical coordinates. The top axis corresponds to the x-coordinate, which is uniformily sampled in the interval $[0, 1]$. The middle and bottom axis present the corresponding r-coordinate when the values $w = 0.5$ and $w = 0.3$, respectively, are plugged into equation (33). We emphasize that the grid is *not* uniformily sampled in the r-coordinate, as we can clearly see in the figure, since $\Delta r_j \equiv r_j - r_{j-1} < \Delta r_{j+1}$.

Since our equations are not covariant under the change of coordinates (33), we must adjust them appropriately. For example, we see that

$$dr = \frac{A}{w}\frac{\cosh\left(\frac{x}{w}\right)}{\sinh\left(\frac{1}{w}\right)}dx \implies \partial_r = \frac{w}{A}\frac{\sinh\left(\frac{1}{w}\right)}{\cosh\left(\frac{x}{w}\right)}\partial_x \ , \tag{34}$$

so that the evolution equations now become

$$\partial_t\Phi = \frac{w}{A}\frac{\sinh\left(\frac{1}{w}\right)}{\cosh\left(\frac{x}{w}\right)}\partial_x\left(\frac{\alpha}{a}\Pi\right) \ , \tag{35}$$

$$\partial_t\Pi = \frac{w}{A}\frac{\sinh\left(\frac{1}{w}\right)}{\sinh^2\left(\frac{x}{w}\right)\cosh\left(\frac{x}{w}\right)}\partial_x\left[\sinh^2\left(\frac{x}{w}\right)\frac{\alpha}{a}\Phi\right] \ , \tag{36}$$

$$\frac{\partial_x\alpha}{\alpha} - \frac{\partial_x a}{a} - \frac{a^2-1}{w\tanh\left(\frac{x}{w}\right)} = 0 \ , \tag{37}$$

$$\frac{\partial_x a}{a} + \frac{a^2-1}{2w\tanh\left(\frac{x}{w}\right)} = 2\pi\frac{A^2}{w\sinh^2\left(\frac{1}{w}\right)}\sinh\left(\frac{x}{w}\right)\cosh\left(\frac{x}{w}\right)\left(\Phi^2+\Pi^2\right) \ . \tag{38}$$

The discretization techniques used for the system above are identical to the ones in Spherical coordinates and will not be repeated here.

2.4 Structure of the evolution

The evolution of the EKG+ADM system of equations is relatively awkward since we are not allowed to use common (and simple) integrators that follow the *method of lines*, such as RK4. The reason for this is that both the Hamiltonian constraint and the polar slicing conditions are *elliptic* equations, while the EKG equations are *hyperbolic* equations. Simply put, the EKG equations are equations that move Φ and Π forward in time based on their values on previous time levels, while the Hamiltonian constraint and polar slicing condition solve for a and α, respectively, based on information on a *single* time level. This makes the integration less efficient, particularly because the Hamiltonian constraint is a non-linear equation from which we are trying to determine A_{j+1}^{n+1}. This means that the equation must be solved on every single gridpoint using a Newton-Raphson solver, for example, which considerably slows down the evolution and complicates the numerical algorithm. The polar slicing condition is not as difficult, it is simply a linear equation that must be solved for α_{j+1}^{n+1} in terms of other known quantities, but also contributes to making the integration more difficult.

During the integration process, we have access to (Φ, Π, a, α) on all spatial points, on the time levels n and $n-1$. This means that a typical integration step is carried out in the following way:

1. Integrate Φ to the time level $n+1$

2. Integrate Π to the time level $n+1$

3. Solve the Hamiltonian constraint to find A at the time level $n+1$; compute a from A

4. Solve the polar slicing condition to find α at the time level $n+1$

5. Set $t_{\text{new}} = (n+1)\Delta t$. If $t_{\text{new}} < t_{\text{max}}$, go to step 1

The summary above ignores quite a few implementation details, such as when and how to apply boundary conditions. We will go over those over the following sections.

2.5   Inner and outer boundary conditions

2.5.1   Inner boundary conditions

Let us first discuss inner boundary conditions, as these can be slightly more confusing to understand, specially since the arguments used by Choptuik are far more technical and obscure. Consider a function $f(t,r)$ which is spherically symmetric. Now what should be the behaviour of this function at $f(t,0)$? It is straightforward to see that, because of spherical symmetry,

$$f(t, -\Delta r) = f(t, +\Delta r) \ , \tag{39}$$

which can then be rewritten as

$$f(t, +\Delta r) - f(t, -\Delta r) = 0 \implies \partial_r f(t,r)|_{r=0} = 0 \ . \tag{40}$$

Notice that this is an *inner* boundary condition, meaning that we are not really imposing anything, we are simply mapping the point $f(t, -\Delta r)$ to another point in the grid, so that all points involved belong to the grid. Because we are imposing the boundary condition on the derivative of the fields, this is a *Neumann boundary condition*. We will then demand that:

$$\partial_r \phi|_{r=0} = 0 \ , \tag{41}$$

$$\partial_r \alpha|_{r=0} = 0 \ . \tag{42}$$

The first of these conditions must be translated in terms of Φ and Π. We impose

$$\Phi(t,0) = 0 \ , \ \ \partial_r \Pi|_{r=0} = 0 \ . \tag{43}$$

For the metric quantity $a(t,r)$, on the other hand, we must impose a different kind of boundary condition. This boundary condition is a direct consequence of our radial gauge,

which, as mentioned before, ensures that a sphere of radius r has proper area $4\pi r^2$, and is given by

$$a(t,0) = 1 . \tag{44}$$

This is a relatively strange boundary condition, which can be viewed as the so-called "elementary flatness condition", which demands that the spacetime is free of conical singularities at the origin.

Box 4: EKG+ADM – Inner boundary conditions

For the EKG+ADM system, we apply the following *inner* boundary conditions:

$$\Phi|_{r=0} = 0 ,$$
$$\partial_r \Pi|_{r=0} = 0 ,$$
$$a|_{r=0} = 1 ,$$
$$\partial_r \alpha|_{r=0} = 0 .$$

2.5.2 Outer boundary conditions

The outer boundary of our computational domain, located at $r = r_{\max}$, with $r_{\max}$ a user specified parameter, has to be treated carefully because using our centered finite difference stencils would require using points *outside* our grid. At this point, then, we will change the finite difference approximation to *backwards* finite difference stencils, namely

$$
\begin{aligned}
(\partial_r f)^n_j &= \frac{3f^n_j - 4f^n_{j-1} + f^n_{j-2}}{2\Delta r} + \mathcal{O}\left(\Delta r^2\right) , \\
(\partial_t f)^n_j &= \frac{3f^n_j - 4f^{n-1}_j + f^{n-2}_j}{2\Delta t} + \mathcal{O}\left(\Delta t^2\right) .
\end{aligned}
\tag{45}
$$

For the scalar field, we will impose *outgoing radiation boundary conditions*, which follow from the case where the scalar field is propagating without being coupled to gravity, i.e. the wave equation in spherical symmetry. The general solution to the spherically symmetric wave equation in spherical coordinates is

$$\phi(t,r) = \frac{F(t-r) + G(t+r)}{r} , \tag{46}$$

where $F(t-r)$ represents an *outgoing* wave and $G(t+r)$ an *ingoing* wave. We will demand that

no extra radiation enters the computational domain at the outer boundary, which translates to the condition

$$\left(\partial_t \left[r\phi(t,r) \right] + \partial_r \left[r\phi(t,r) \right] \right)\big|_{r=r_{\max}} = 0 \ , \tag{47}$$

at the outer boundary. This introduces a complication, since this condition cannot be written in terms of Φ and Π alone. The easiest way to account for this is to impose the condition to ϕ itself, then compute Φ and Π using their definitions. The discretization of this equation yields the outer boundary condition

$$\phi_J^{n+1} = \left(\frac{3}{\Delta t} + \frac{2}{r_J} + \frac{3}{\Delta r} \right)^{-1} \left[\frac{4\phi_J^n - \phi_J^{n-1}}{\Delta t} + \frac{4\phi_{J-1}^{n+1} - \phi_{J-2}^{n-1}}{\Delta r} \right] \ , \tag{48}$$

where the index J corresponds to $r_{\max}$. Note that this is also a $\mathcal{O}\left(\Delta r^2 + \Delta t^2 \right)$ approximation.

The desired boundary condition for α is that $\lim_{r \to r_{\max}} \alpha \to 1$, i.e. asymptotic flatness. To obtain this, we must also consider our inner boundary condition $\partial_r \alpha|_{r=0} = 0$. Note that this condition can be interpretedd as implying that

$$\alpha(t,0) = C \ , \tag{49}$$

where C is an arbitrary constant. We choose to set $C = 1$ for simplicity, but this is not a physical boundary condition. The physical boundary condition is asymptotic flatness. In order to ensure that asymptotic flatness is enforced, we perform a *rescaling of the lapse function* following Choptuik's prescription. First, notice that the "evolution equation" for the lapse function (i.e. the polar slicing condition) can be written in the form

$$\alpha_{j+1}^n = \alpha_j^n \left(\frac{1 - \Delta r d}{1 + \Delta r d} \right) \ , \tag{50}$$

where

$$d = \frac{1 - \frac{b^2}{4}}{r_{j+1/2}} - \frac{c}{b\Delta r} \ , \tag{51}$$

and

$$b = a_{j+1}^n + a_j^n \quad \text{and} \quad c = a_{j+1}^n - a_j^n \ . \tag{52}$$

Notice, now, that the polar slicing condition is homogeneous in α, meaning that if we multiply α *on the entire hypersurface of constant time* by a constant, then the polar slicing condition is still satisfied. To ensure asymptotic flatness and that no signals propagate faster than the speed of light, we choose this constant to be

$$\kappa = \min_{0 \leq j \leq J} \left(\frac{a_j^n}{\alpha_j^n} \right) . \tag{53}$$

This rescaling typically sets $\alpha(t, r_{\max}) = a(t, r_{\max})$, which means that we are dealing with a metric that does not behave like the Schwarzschild metric, where we have $\alpha = a^{-1}$, except when $a = 1$.

Box 5: EKG+ADM – Outer boundary conditions

For the EKG+ADM system, we apply the following *outer* boundary conditions:

$$\phi_J^{n+1} = \left(\frac{3}{\Delta t} + \frac{2}{r_J} + \frac{3}{\Delta r} \right)^{-1} \left[\frac{4\phi_J^n - \phi_J^{n-1}}{\Delta t} + \frac{4\phi_{J-1}^{n+1} - \phi_{J-2}^{n-1}}{\Delta r} \right] ,$$

$$\kappa = \min_{0 \leq j \leq J} \left(\frac{a_j^{n+1}}{\alpha_j^{n+1}} \right) ,$$

$$\alpha_j^{n+1} \to \kappa \alpha_j^{n+1} .$$

2.6 Initial condition

The initial condition for the scalar field is

$$\phi(0, r) = \eta \exp \left[-\frac{(r - r_0)^2}{\delta^2} \right] ,$$
$$\partial_t \phi(0, r) = 0 . \tag{54}$$

Typically the parameters r_0 and δ are fixed, while the parameter η, the amplitude of the initial pulse, varies on different runs of the code. This is the parameter p we mentioned, for which we wish to find the critical value $p^* = \eta_*$ that separates solutions with black hole formation from those with total dispersion.

In terms of Φ and Π, the inital condition reads

$$\Phi(0, r) = -2\frac{(r - r_0)}{\delta^2}\eta \exp \left[-\frac{(r - r_0)^2}{\delta^2} \right] ,$$
$$\Pi(0, r) = 0 . \tag{55}$$

To obtain the initial values of a and α we must solve the constraints.

Although we have shown the initial data used by Matt Choptuik in his PhD thesis [4] and his

original work [1], we will choose different values for the free parameters (r_0, δ). As pointed out by Thomas Baumgarte [5], Choptuik's choice for (r_0, δ) lead to initial conditions which are ill-defined at the origin, as illustrated in figure 3. The radial derivative of the scalar field, $\Phi = \partial_r \phi$, does not go smoothly to zero at the origin, but has a "kink" instead. This is a consequence of imposing Neumann boundary conditions at the origin, but having an initial condition which is incompatible with this boundary condition when $r_0 \neq 0$.
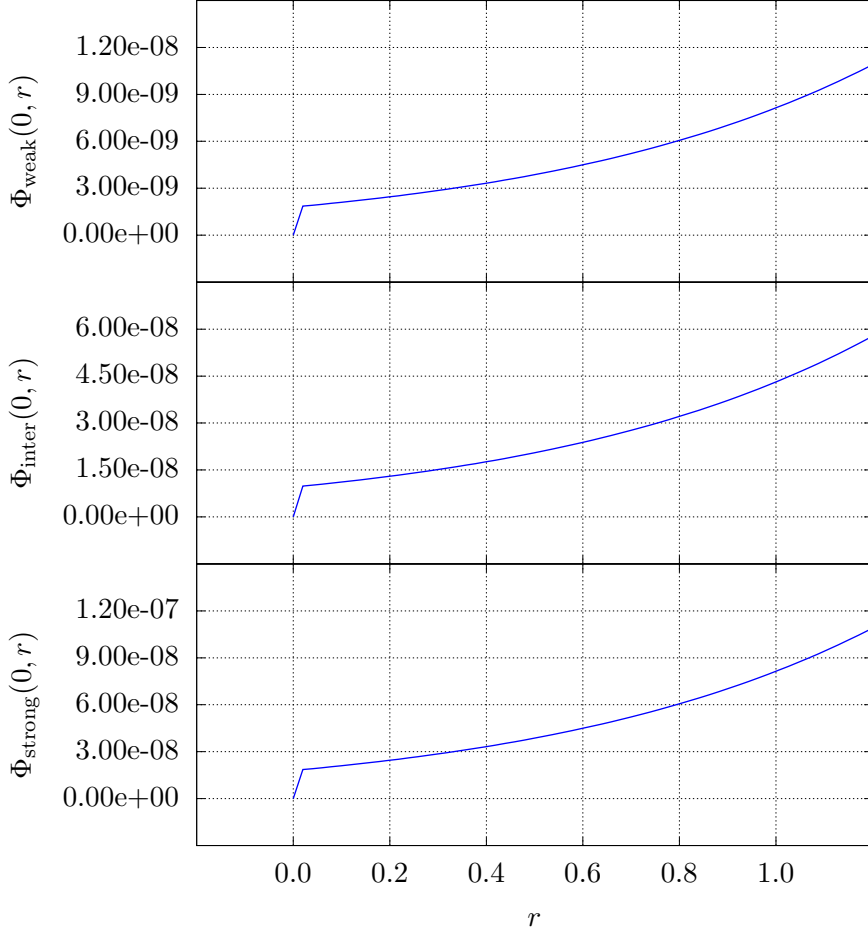
Figure 3: This figures shows the problem with the initial condition set by Choptuik in his original studies. There is a kink in the first derivative of the scalar field at the origin, namely the variable Φ.

Baumgarte has proposed a fix which he has already used himself in his studies of gravitational collapse of massless scalarfields [6]. It is a very simple fix, which consists of changing the parameters r_0 and δ appropriately. The simplest approach is to set $r_0 = 0$ and $\delta = 1$, which then results in the initial condition

$$\phi(0, r) = \eta \exp\left(-r^2\right) ,$$

$$\Phi(0, r) = -2r\eta \exp\left(-r^2\right) , \tag{56}$$

$$\Pi(0, r) = 0 .$$

This condition then guarantees that Φ is both zero and smooth at the origin. Alternatively, one could multiply $\phi(0, r)$ by r^n with $n \geq 2$, which then also guarantees that $\phi(0, r = 0) = 0$.

2.7 The `SFcollapse1D` code

Here is what `SFcollapse1D` does in pseudocode:

---

1 begin *Initial condition*

2   Set the initial condition for ϕ_j^0, Φ_j^0, and Π_j^0;

3   Impose inner boundary conditions to Φ_0^0, a_0^0, and α_0^0;

4   Solve the Hamiltonian constraint to determine a_j^0;

5   Solve the polar slicing condition to determine α_j^0;

6   Perform the rescaling of the lapse function;

7 begin *Initial data*

8   Apply inner boundary conditions to set $\Phi_0^{1/2}$, $a_0^{1/2}$, and $\alpha_0^{1/2}$;

9   **for** $j = 1$ **to** $N_r - 1$ **do**

10   **if** $j = 1$ **then** start by computing $\phi_0^{1/2}$;

11   Perform a half-step integration, compute $\phi_j^{1/2}$, $\Phi_j^{1/2}$, and $\Pi_j^{1/2}$;

12   Apply outgoing radiation boundary conditions to $\phi_{N_r}^{1/2}$;

13   Apply inner boundary conditions to find $\Pi_0^{1/2}$;

14   Compute $\Phi_{N_r}^{1/2}$ and $\Pi_{N_r}^{1/2}$;

15   **for** $j = 0$ **to** N_r **do**

16   Solve the Hamiltonian constraint to determine $a_j^{1/2}$;

17   Solve the polar slicing condition to determine $\alpha_j^{1/2}$;

18   Perform the rescaling of the lapse function;

19   Apply inner boundary conditions to set Φ_0^1, a_0^1, and α_0^1;

20   **for** $j = 1$ **to** $N_r - 1$ **do**

21   **if** $j = 1$ **then** start by computing ϕ_0^1;

22   Perform a single-step integration, compute ϕ_j^1, Φ_j^1, and Π_j^1;

23   Apply outgoing radiation boundary conditions to $\phi_{N_r}^1$;

24   Apply inner boundary conditions to find Π_0^1;

25   Compute $\Phi_{N_r}^1$ and $\Pi_{N_r}^1$;

26   **for** $j = 0$ **to** N_r **do**

27   Solve the Hamiltonian constraint to determine a_j^1;

28   Solve the polar slicing condition to determine α_j^1;

29   Perform the rescaling of the lapse function;

30 begin *Evolution*

31   **while** $t < t_{\text{final}}$ **do**

32   Apply inner boundary conditions to set Φ_0^n, a_0^n, and α_0^n;

33   **for** $j = 1$ **to** $N_r - 1$ **do**

34   **if** $j = 1$ **then** start by computing ϕ_0^n;

35   Compute ϕ_j^n, Φ_j^n, and Π_j^n;

36   Apply outgoing radiation boundary conditions to $\phi_{N_r}^n$;

37   Apply inner boundary conditions to find Π_0^n;

38   Compute $\Phi_{N_r}^n$ and $\Pi_{N_r}^n$;

39   **for** $j = 1$ **to** N_r **do**

40   Solve the Hamiltonian constraint to determine a_j^n;

41   Solve the polar slicing condition to determine α_j^n;

42   Perform the rescaling of the lapse function;

Algorithm 1: The `SFcollapse1D` program's pseudocode.

2.8 Results

2.8.1 The different field regimes

In this section we present results from different runs in the so-called *weak* and *strong* field regimes. We emphasize here that the results presented in this section were not obtained with accuracy and stability in mind, but simply to illustrate the different regimes. This means that our grid choices are not meant to be used during production runs, since they underesolve the structures that emerge once the scalar field propagates and interacts with the underlying geometry.

Throughout this section we fix the parameters $r_0 = 0$ and $\delta = 1$, so that η is the parameter that will vary and allow us to obtain results in different regimes. Although we are evolving the set of variables $(\phi, \Phi, \Pi, a, \alpha)$, we will be interested in looking only at the scalar field $\phi(t, r)$, the lapse function $\alpha(t, r)$, and the *mass-aspect function*, $M(t, r)$, which is defined in analogy to the Schwarzschild metric

$$a^2(t,r) \equiv \frac{1}{1 - \frac{2M(t,r)}{r}} \implies M(t,r) = \frac{r}{2}\left[1 - \frac{1}{a^2(t,r)}\right] . \tag{57}$$

The weak field regime is obtained by setting η to a small value.[2] In the run whose results are presented in figures 4, 5, and 6, we have set $\eta = 0.05$. In this regime, the metric quantities α and a differ at most $\sim 2\%$ from flat space, the deviation being more prominent for the lapse than the radial metric. Because of this, the backreaction from the geometry on the scalar field is negligible and we see it propagating as if it was not coupled to gravity at all, i.e. just a simple scalar wave in spherical coordinates.

---

[2]A natural question is then "small when compared to what"? The answer to this question is meant to be "small when compared to η_*", but even that is not really satisfactory since 1) we do not know η_* *a priori* and 2) even if we are given η_* it is not obvious how to choose η. Indeed, the best answer to this question is that we empirically determine the value of η by finding a solution that produces a spacetime which is almost flat throughout the entire run.
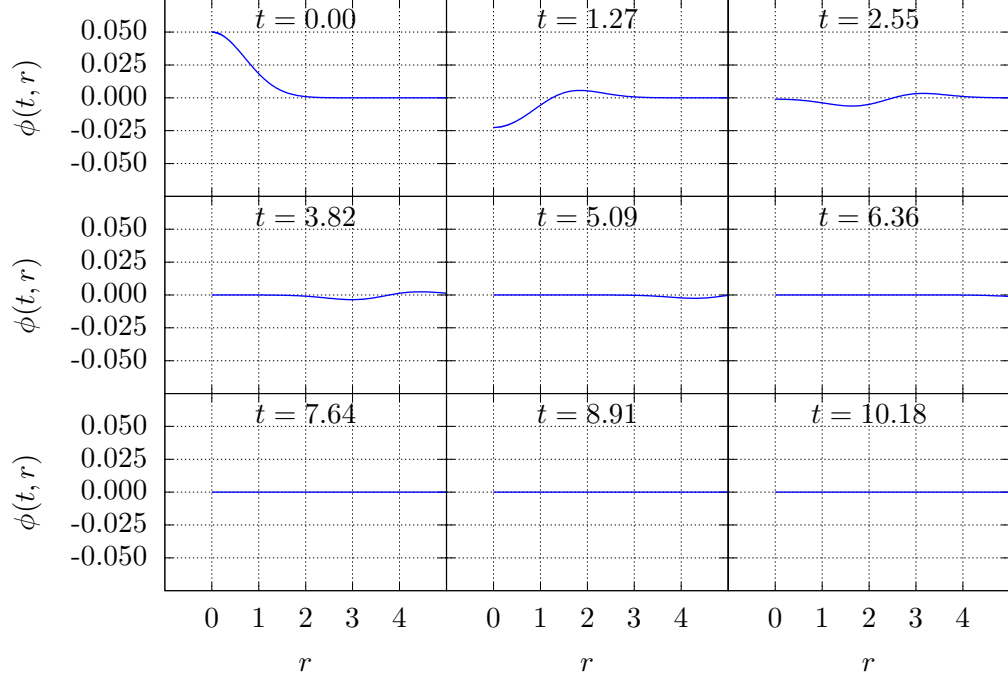
Figure 4: Weak field results for the scalar field $\phi(t,r)$. The parameters of the run are $\eta = 0.05$, $r_0 = 0$, $\delta = 1$, $r_{\max} = 64$, $w = 0.15$, and $N_r = 640$.
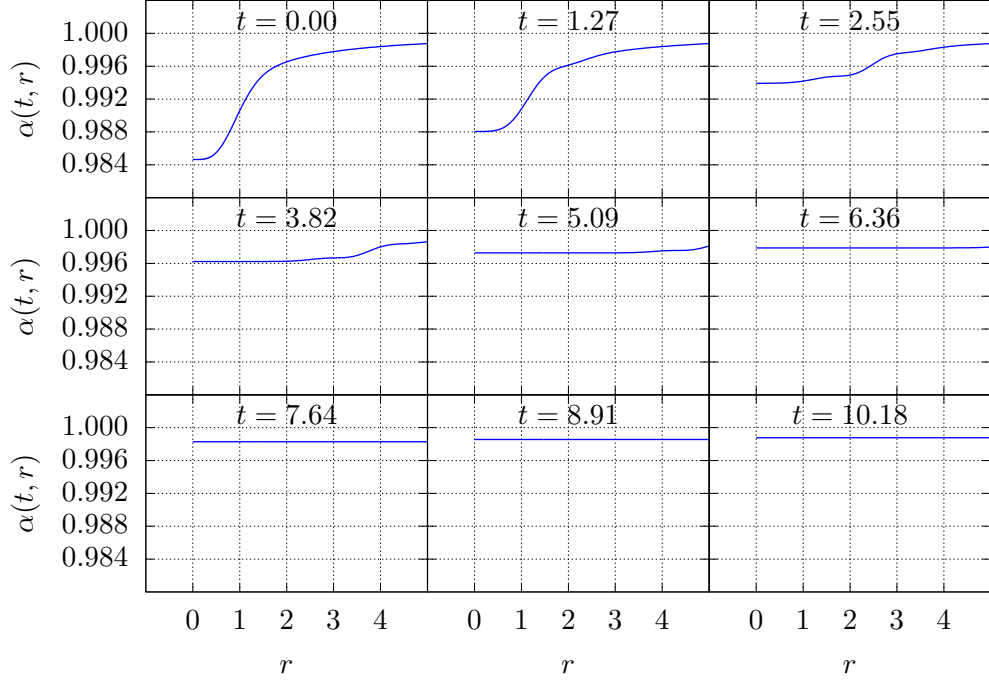

Figure 5: Weak field results for the lapse function $\alpha(t,r)$. The parameters of the run are $\eta = 0.05$, $r_0 = 0$, $\delta = 1$, $r_{\max} = 64$, $w = 0.15$, and $N_r = 640$.
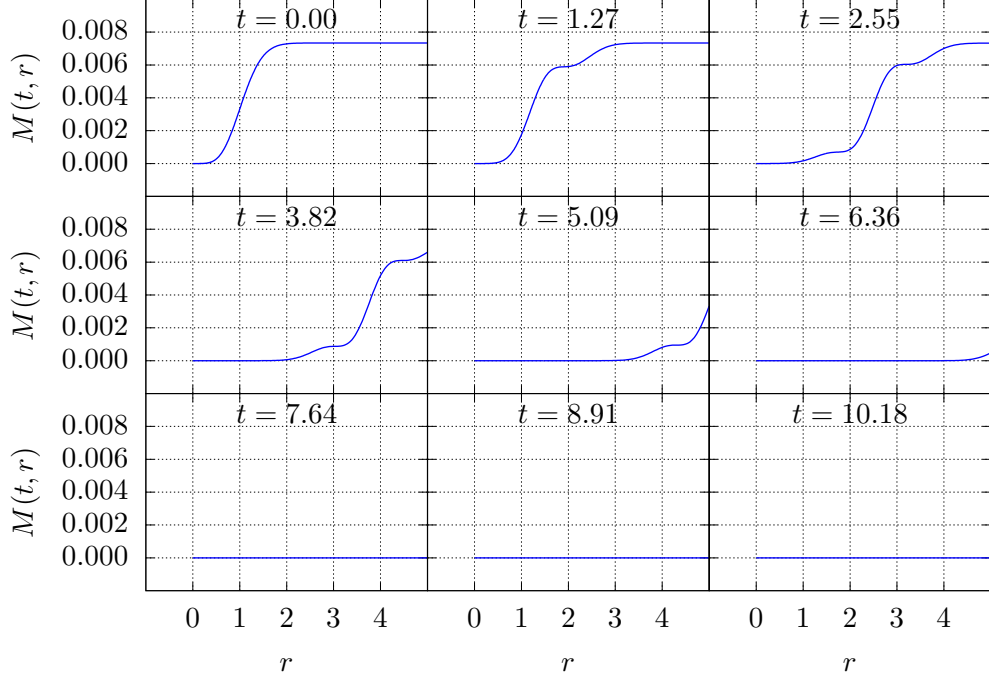
Figure 6: Weak field results for the mass-aspect function $M(t,r)$. The parameters of the run are $\eta = 0.05$, $r_0 = 0$, $\delta = 1$, $r_{\max} = 64$, $w = 0.15$, and $N_r = 640$.

For the strong field results we have set $\eta = 0.6$. This regime is characterized by total collapse, meaning that the scalar field energy is strong enough to curve spacetime to the point where a singularity emerges. If the rresolution of the run is sufficiently high, it is possible to prevent the simulation from crashing immediately after black hole formation. However, our resolution was not enough to keep this from happening nor from preventing that energy "leaked" out of the black hole interior after its formation.

The lapse function goes to zero[3] in this regime, which is a statement that around that region there is virtually no proper time being elapsed between one hypersurface of constant time and the next. This is known as the *freezing of the lapse function*, and is a very useful feature to detect black hole formation.

The strong field regime results are presented in figures 7, 8, and 9. Figure 7 shows clearly that no time is passing for the scalar field after it collapses, since its evolution gets frozen. The freezing of the lapse function is evident in figure 8, while the mass of the black hole formed (in code units) can be seen as the plateau of the function $m(t,r)$ in figure 9.

---

[3]In the actual code the lapse reaches a very small value, below 10^{-3} for example, which is enough for us to characterize black hole formation.
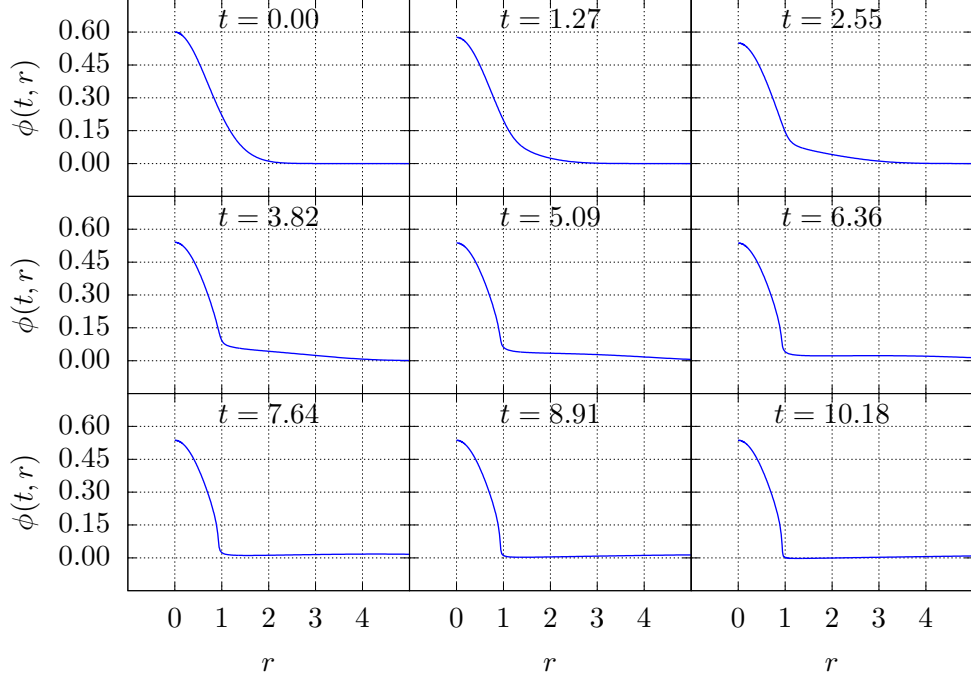
Figure 7: Strong field results for the scalar field $\phi(t, r)$. The parameters of the run are $\eta = 0.6$, $r_0 = 0$, $\delta = 1$, $r_{\max} = 64$, $w = 0.15$, and $N_r = 640$.
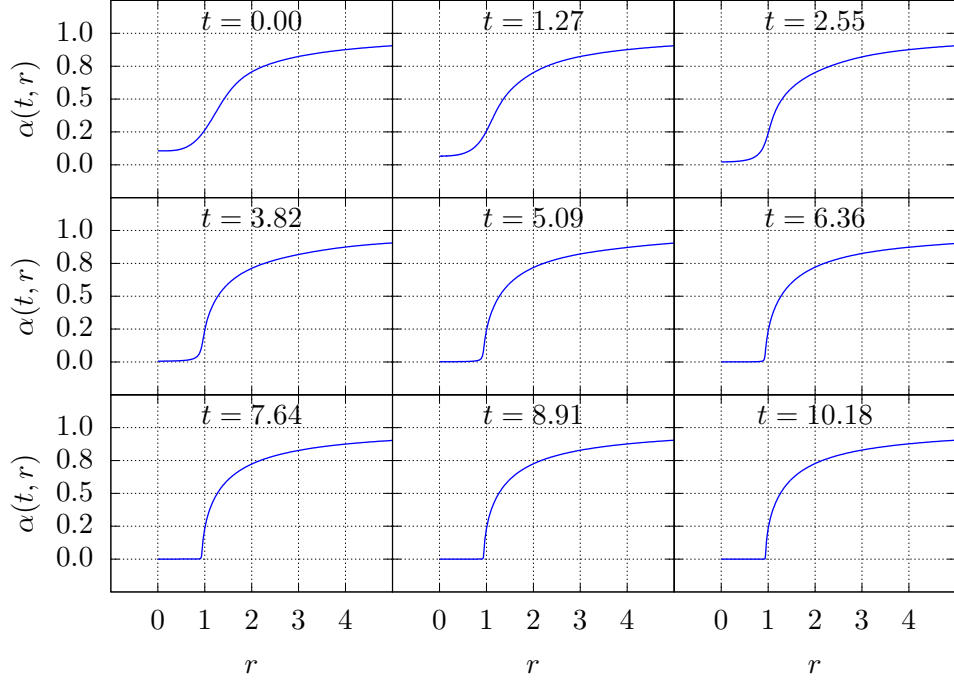

Figure 8: Strong field results for the lapse function $\alpha(t, r)$. The parameters of the run are $\eta = 0.6$, $r_0 = 0$, $\delta = 1$, $r_{\max} = 64$, $w = 0.15$, and $N_r = 640$.
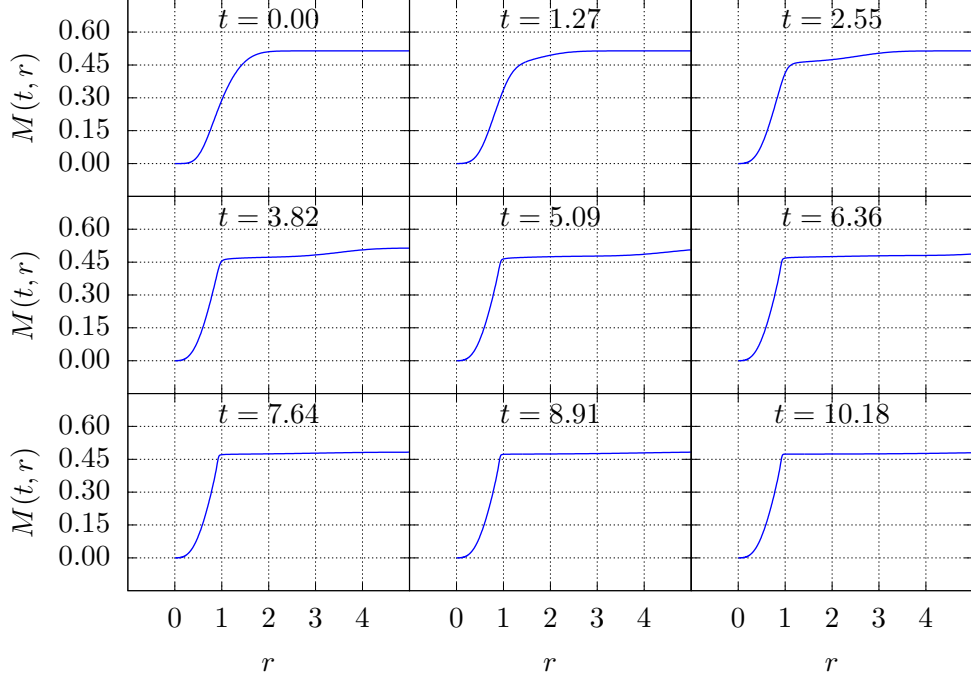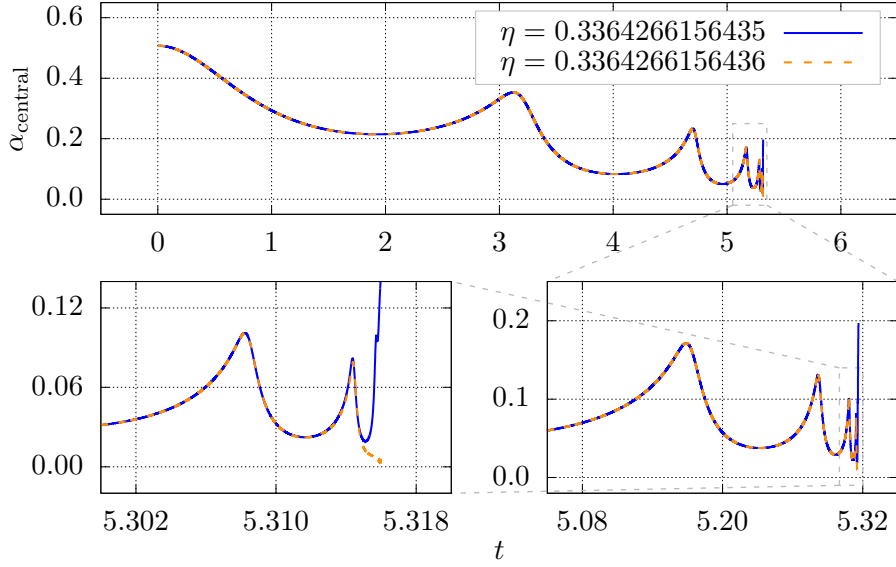
Figure 9: Strong field results for the mass-aspect function $M(t, r)$. The parameters of the run are $\eta = 0.6$, $r_0 = 0$, $\delta = 1$, $r_{\max} = 64$, $w = 0.15$, and $N_r = 640$.

2.8.2 Critical phenomena

Figure 10: α_{central} results near criticality using a different grid setup. The simulation parameters used were $N_r = 320$, $w = 0.08$, and $r_{\max} = 16$. Note that we have fine-tuned the critical parameter to $\delta\eta \sim 10^{-13}$.
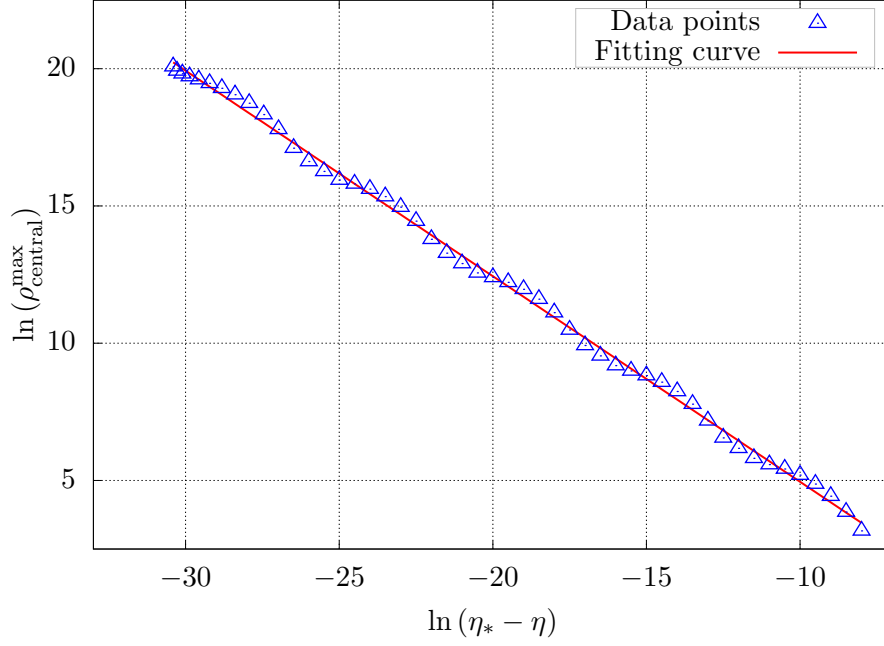
Figure 11: Critical exponent behaviour for several subcritical data runs. The plot shows the maximum central density as a function of the logarithmic difference of the critical parameter η_* and the run parameter η. The fitting function chosen was $\rho_{\text{central}}^{\max} \sim |\eta_* - \eta|^{-2\gamma}$, resulting in the critical exponent $\gamma \approx 0.3746$, in excellent agreement with the literature.
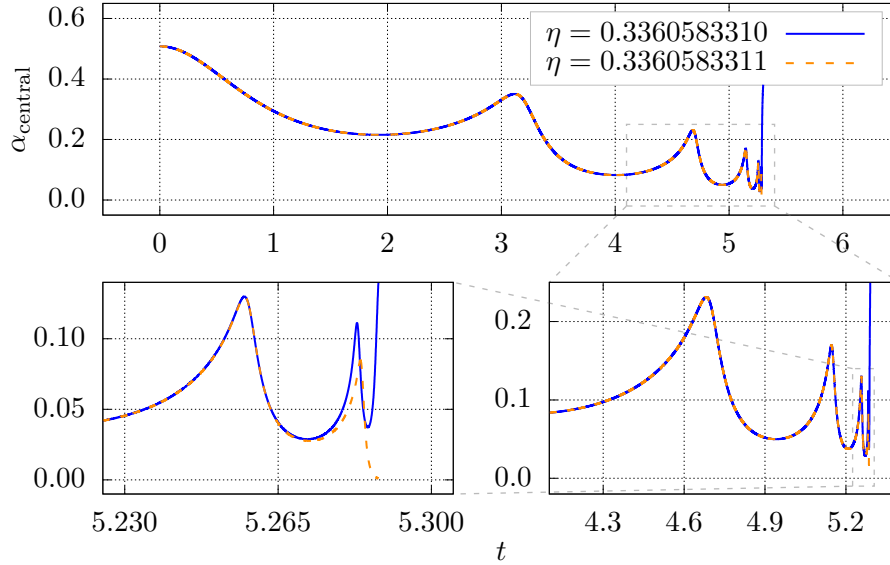

Figure 12: α_{central} results near criticality. The results below have been found by first finding initial values that result in full dispersal and black hole formation, respectively, and then fine tuning the value of η using bisection. The simulation parameters used were $N_r = 960$, $w = 0.11$, and $r_{\max} = 16$. Note that we have fine-tuned the critical parameter to $\delta\eta \sim 10^{-10}$.

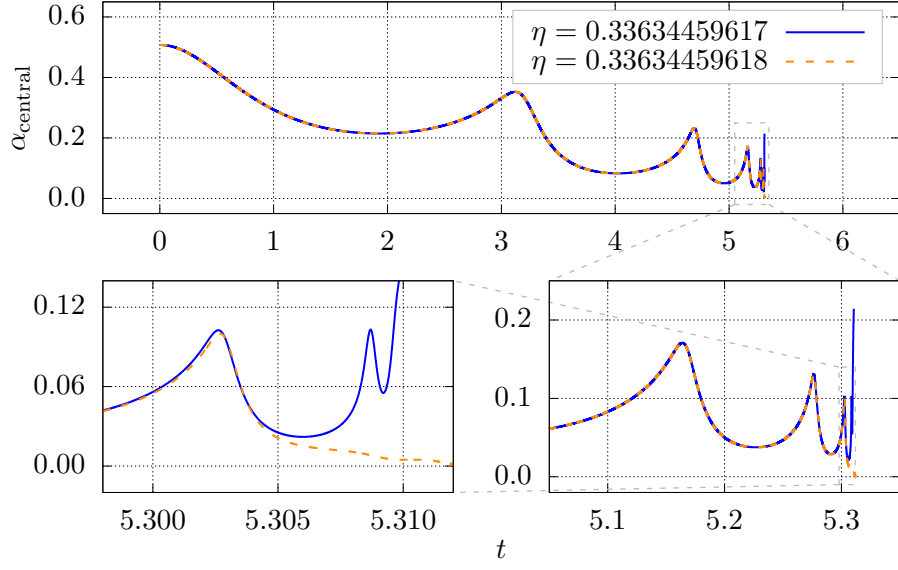Figure 13: α_{central} results near criticality using a different grid setup. The simulation parameters used were $N_r = 320$, $w = 0.09$, and $r_{\text{max}} = 16$. Note that we have fine-tuned the critical parameter to $\delta\eta \sim 10^{-11}$.

References

[1] Matthew W. Choptuik. "Universality and scaling in gravitational collapse of a massless scalar field". In: *Phys. Rev. Lett.* 70 (1 Jan. 1993), pp. 9–12. DOI: 10.1103/PhysRevLett.70.9. URL: https://link.aps.org/doi/10.1103/PhysRevLett.70.9.

[2] Richard L. Arnowitt, Stanley Deser, and Charles W. Misner. "Dynamical Structure and Definition of Energy in General Relativity". In: *Phys. Rev.* 116 (1959), pp. 1322–1330. DOI: 10.1103/PhysRev.116.1322.

[3] Thomas W. Baumgarte and Stuart L. Shapiro. *Numerical Relativity: Solving Einstein's Equations on the Computer*. Cambridge University Press, 2010. DOI: 10.1017/CBO9781139193344.

[4] Matthew William Choptuik. "A study of numerical techniques for radiative problems in general relativity". PhD thesis. University of British Columbia, 1986. DOI: http://dx.doi.org/10.14288/1.0085044. URL: https://open.library.ubc.ca/cIRcle/collections/831/items/1.0085044.

[5] T. Baumgarte. Private communication. July 3, 2019.

[6] Thomas W. Baumgarte. "Aspherical deformations of the Choptuik spacetime". In: *Physical Review D* 98.8 (Oct. 2018). ISSN: 2470-0029. DOI: 10.1103/physrevd.98.084012. URL: http://dx.doi.org/10.1103/PhysRevD.98.084012.